

# Soft Sensing Shirt for Shoulder Kinematics Estimation

Yichu Jin<sup>1,2</sup>, Christina M. Glover<sup>1</sup>, Haedo Cho<sup>1,2</sup>, Oluwaseun A. Araromi<sup>1,2</sup>, Moritz A. Graule<sup>1,2</sup>, Na Li<sup>1</sup>, Robert J. Wood<sup>1,2</sup>, and Conor J. Walsh<sup>1,2</sup>

**Abstract**— Soft strain sensors have been explored as an unobtrusive approach for wearable motion tracking. However, accurate tracking of multi degree-of-freedom (DOF) noncyclic joint movements remains a challenge. This paper presents a soft sensing shirt for tracking shoulder kinematics of both cyclic and random arm movements in 3 DOFs: adduction/abduction, horizontal flexion/extension, and internal/external rotation. The sensing shirt consists of 8 textile-based capacitive strain sensors sewn around the shoulder joint that communicate to a customized readout electronics board through sewn micro-coaxial cables. An optimized sensor design includes passive shielding and demonstrates high linearity and low hysteresis, making it suitable for wearable motion tracking. In a study with a single human subject, we evaluated the tracking capability of the integrated shirt in comparison with a ground truth optical motion capture system. An ensemble-based regression algorithm was implemented in post-processing to estimate joint angles and angular velocities from the strain sensor data. Results demonstrated root mean square errors (RMSEs) less than 4.5° for joint angle estimation and normalized root mean square errors (NRMSEs) less than 4% for joint velocity estimation. Furthermore, we applied a recursive feature elimination (RFE)-based sensor selection analysis to down select the number of sensors for future shirt designs. This sensor selection analysis found that 5 sensors out of 8 were sufficient to generate comparable accuracies.

## I. INTRODUCTION

Human motion tracking is desirable for many applications such as animation, sports, rehabilitation, and biomechanics study. It focuses on estimating positions and orientations of various body segments. With the recent wearable sensor development, motion tracking in non-lab-constrained environments becomes possible and opens up many applications. In the field of wearable robotics, continuous tracking of joint angles and velocities enables robotic assistive devices to autonomously operate in sync with the user's motion or intention [1], [2].

To achieve motion tracking, various approaches have been proposed including optical motion capture systems, inertial-measurement units (IMUs), and soft strain sensors. Optical motion capture has been considered the gold standard because of its high accuracy, but it is generally expensive and constrained to lab environments. IMU systems have overcome this space limitation but have often suffered from integration drift, especially in the plane perpendicular to gravity. To reduce drift, many sensor fusion schemes involving multiple

types of sensors have been proposed [3], [4]. Most of the proposed methods rely on magnetometers [5], [6], whose signals are susceptible to environmental ferromagnetic materials [7]. In dealing with the magnetic disturbances, existing approaches involve limiting the contribution of the magnetometer measurement [8] or actively updating magnetic field directions [9], [10]. In an effort to achieve unobtrusive wearable systems with minimal signal conditioning, soft strain sensors that are highly stretchable and compliant have been explored as an alternative wearable motion tracking approach. A soft strain sensing approach tracks human kinematics by measuring the skin or textile deformation due to body motion and then mapping this information to the inducing body movement.

Previous work in using soft strain sensors for motion tracking have mostly focused on detecting single degree-of-freedom (DOF) joint motions. For example, existing lower extremity sensing suits tracked motions of hips, knees, and ankles in the sagittal plane for gait detection [11]-[13] or kinematics analysis [14], [15]. Additionally, soft strain sensors were attached over finger joints [16]-[18] or the elbow joint [19] to measure degrees of flexion and extension. For tracking a single DOF, a single sensor with linear regression is often sufficient to accurately represent the signal-to-motion relationship. To track a joint with multiple DOFs, multiple sensors with more sophisticated algorithms are needed. In [20], two piezoresistive soft sensors and a geometry-based calibration method were used to detect two-DOF shoulder motions. Comparing to an optical motion capture system, this study achieved root mean square errors (RMSEs) less than 10° for rhythmic shoulder flexion and shoulder abduction. In other work, [21] demonstrated simultaneous tracking of multiple joints including shoulders, elbows, hip, and knees. Through the use of 20 microfluidic soft sensors and a deep learning algorithm, a full body 3-D skeleton was reconstructed with the overall estimation RMSE of 29.5 mm for three repetitive motions: squat, bend and reach, and windmill.

Despite exciting proof of concept demonstrations, there remain limitations to enable multi-DOF tracking with soft strain sensors to become practical enough for real-world applications. Sensor nonlinearity and hysteresis have made it challenging to accurately estimate body motion, especially in the multi-sensor configuration. It was recently proposed to calibrate these sensor characteristics using deep learning [22], [23]. Through the use of recurrent neural networks, temporal sequences of past sensor signals were recorded to calibrate the sensor's nonlinearity and hysteresis. Such temporal sequence modeling learnt the sensor signal's history dependency and enabled tracking of rhythmic body movements [13], [21]. However, accurate tracking of non-cyclic multi-DOF joint movements has yet to be demonstrated. Moreover, most

\*This research was supported by the Tata-Harvard Alliance, National Science Foundation EFRI Award (#1830896).

<sup>1</sup> John A. Paulson School of Engineering and Applied Sciences, Harvard University, Cambridge, MA 02138, USA

<sup>2</sup> Wyss Institute for Biologically Inspired Engineering, Harvard University, MA 02138, USA

Corresponding author email: [walsh@seas.harvard.edu](mailto:walsh@seas.harvard.edu) (C. J. Walsh)

multi-DOF tracking studies have omitted tracking joint internal/external rotation. This is because the skin or textile deformation induced by movements in different DOFs is often coupled and only the net result can be measured. Since internal/external rotation introduces a smaller amount of deformation, it is more challenging to decouple and track such joint rotation compared to other DOFs. To overcome this challenge, a large number of high-resolution sensors around the multi-DOF joint with a data-driven rotation estimation algorithm could be a viable solution.

In this paper, we present a soft sensing shirt (Fig. 1) that is capable of accurately tracking shoulder joint kinematics for both cyclic and random arm movements in 3 DOFs, including rotations around the longitudinal axis of the arm. The sensing shirt consists of 8 textile-based strain sensors sewn around the shoulder joint. The presented capacitive sensor design demonstrated high linearity, low hysteresis, and enhanced immunity to parasitic capacitance, making it suitable for wearable multi-DOF tracking. Sensors and cables were integrated into the shirt using industry-standard sewing machines and processes. Sensor signals were read through a customized electronics board and post-processed with an ensemble-based regression algorithm to estimate shoulder joint angles and angular velocities. The high sensor redundancy guaranteed low estimation errors but complicated shirt design and computation. To simplify future sensing shirt design, we conducted a recursive feature elimination (RFE)-based sensor selection analysis to downsize the number of required sensors.

## II. SENSOR DESIGN AND FABRICATION

### A. Design and Principle of Operation

The proposed sensors were based on our previous work [24]. As shown in Fig. 2, this fabric-silicone composite sensor was composed of two silicone dielectric layers (Dragon Skin FX Pro, SmoothOn) sandwiched between three silver-coated knit textile electrode layers (Shieldex Medtex P130+B, V Technical Textiles). By grounding the top and bottom electrodes, the middle electrode provides the sensing signal and is passively shielded from parasitic capacitance,

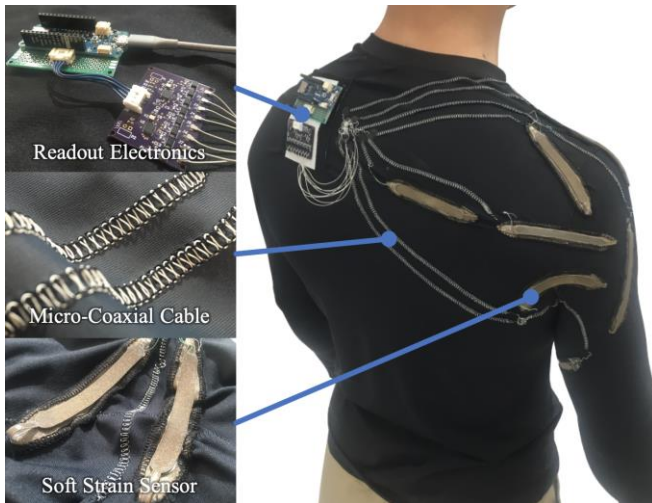


Fig. 1. Overview of the soft sensing shirt with zoom-ins on portable readout electronics (top), sewn micro-coaxial cable (middle), and sewn capacitive soft strain sensors (bottom)

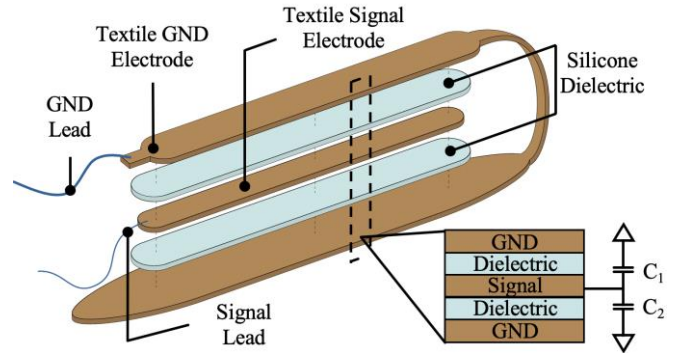


Fig. 2. Layered diagram of the sensor design with scheme of sensor working principles

especially the human body capacitance. To reduce the parasitic fringe capacitance, the ground (GND) electrodes were designed larger than the embedded signal electrode. Dimensions of the sensor were 17 mm wide and 100 mm long with a signal area of 5 mm x 70 mm, a dielectric thickness of 250  $\mu\text{m}$ , and total sensor thickness of 2 mm. The extra footprint of the bottom ground electrode provided sensor sewability.

The sensor's capacitance is determined by the conductor area, the insulator thickness, and the insulator dielectric properties. We assumed that the dielectric properties remained unchanged under deformation, and thus changes in conductor and insulator geometries dominated capacitance changes. As the sensor is strained, its electrode area increases and dielectric thickness decreases, thus increasing sensor capacitance. In our three-electrode configuration, the sensor was considered as two parallel capacitors,  $C_1$  and  $C_2$  (Fig. 2 inset). Since the two silicone dielectric layers were fabricated with the same thickness using the same material,  $C_1$  and  $C_2$  were assumed to be identical. These principles can be represented as:

$$\Delta C = \Delta C_1 + \Delta C_2 = 2\varepsilon_0\varepsilon_r(\Delta A/\Delta d)$$

$\Delta C$  is the change in sensor capacitance,  $\varepsilon_0$  and  $\varepsilon_r$  are vacuum permittivity and relative permittivity of the silicone dielectric, respectively, and  $\Delta A$  and  $\Delta d$  are changes in electrode area and dielectric thickness, respectively.

### B. Fabrication

As shown in Fig. 3, sensors were fabricated using a stencil-based layered fabrication process. First, conductive fabric and stencil materials (P004, Stencil Ease) were cut with a laser to make the outlines of textile electrodes and the stencil layer. As shown in Fig. 3A, the ground electrode and the stencil layer were aligned and stacked on an acrylic base using alignment pins. The ends of the signal leads (2936 SL005, Alpha Wire) were stripped and sewn to the signal electrodes. The signal connections were made before adding the signal electrode to the stack so both the signal electrode and signal connection would be encapsulated in silicone to prevent them from shorting to the ground layer. The silicone dielectric was then casted over the extruded stencil with an automatic thin film applicator (4340, Elcometer Inc). Next, the signal electrode layer was placed on top and the stack was cured in an oven at 60°C for 20 mins. After the silicone was cured, individual sensors were peeled away from the stencil base, folded, and adhered with a thin casting of silicone (Fig. 3B).

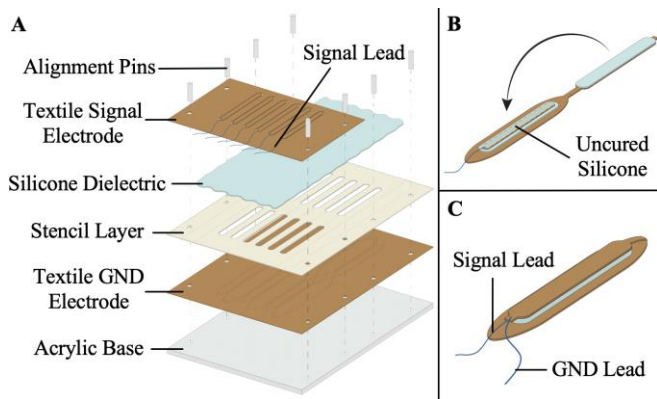


Fig. 3. Stencil based fabrication process of the soft strain sensor.

Lastly, as shown in Fig. 3C, the ground lead (2936 SL005, Alpha Wire) was stripped and sewn through both the top and bottom ground electrodes.

By adopting laser cutting and thin film application processes, this fabrication procedure is precise, rapid, and repeatable. Due to the size constraint of the film applicator used, a maximum of 6 sensors could be fabricated in one batch; however, this number could be scaled up by using a larger applicator.

### III. SENSOR CHARACTERIZATION

#### A. Methods

The capacitive sensors used in the sensing shirt were characterized at room temperature using (1) an extension test and (2) a cyclical load test. Individual sensors were sewn to inextensible textile straps to facilitate the experiments. Synchronized mechanical and electrical data were collected using a mechanical tester (Instron 5544A, Instron) and a capacitance meter (Model 3000, GLK Instruments). The characterization setup is shown in Fig. 4A.

1) *Extension Test*: To test the sensor's electrical and mechanical characteristics, a sensor was strained by 50% and returned to its original length with capacitance, force, and extension values recorded. 50% strain was chosen to mimic the maximum amount of skin deformation observed around the shoulder joint during natural arm movements [25]. To simulate the sensor response at different arm movement speeds, the extension test was repeated 3 times at speeds of 6, 12, and 24 mm/sec (tester mechanical limit). To understand the sensor limitations, a failure test was conducted by stretching the sensor to 250% at the speed of 24 mm/sec.

2) *Cyclical Load Test*: The sensor's fatigue performance was evaluated by cyclically straining the sensor to 50% for 1000 cycles at the speed of 24 mm/sec with a triangle wave profile. Sensors were pre-conditioned prior to testing with 20 cycles at test conditions to mitigate the effect of plastic deformation in the fabric-silicone composite [24].

#### B. Results

(1) *Extension Test*: The sensor's electrical response was evaluated using gauge factor (GF), which described sensor sensitivity and was calculated by dividing  $\Delta C$  by the sensor capacitance at rest length ( $C_0$ ). As shown in Fig. 4B, the tested sensor exhibited high linearity and nearly no hysteresis in its

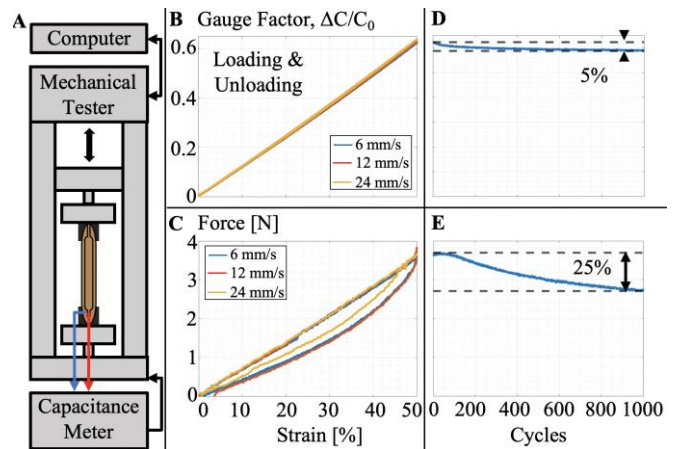


Fig. 4. (A) Illustration of the sensor characterization setup. (B) and (C) show the electrical and mechanical results of the extension test. (D) and (E) show the electrical and mechanical results of the cyclical load test. Note: (B) and (C), (D) and (E) share x-axis. (B) and (D), (C) and (E) share y-axis.

electrical response. Also, the electrical response was velocity independent. These characteristics implied that, when integrated into a garment, the sensor's capacitance would be unaffected by motion history or motion speed, making the proposed sensor suitable for wearable motion tracking.

Regarding the sensor's mechanical response, Fig. 4C shows that stretching the sensor to 50% strain required a maximum force of 3.8 N. To identify possible restrictive impact on normal shoulder kinematics, the maximum force was converted to the expected additive joint torque and compared to the maximum biological joint torque. As an example, a 99<sup>th</sup> percentile male was expected to have a shoulder joint radius of 0.058 m [26]. Assuming the sensor applied force at a moment-arm equal to the joint radius, the expected additive torque would be 0.22 Nm which was 0.23% of the maximum shoulder joint torque reported in literature [27]. This small percentage indicated the sensor's minimal impact on shoulder joint movement. Additionally, some hysteresis was observed, and the amount of mechanical hysteresis was speed dependent. These characteristics implied that the sensing shirt would restrict differently depending on movement speeds and directions. However, the sensor restrictiveness was small enough for the mechanical hysteresis to not impact the wearer.

The failure test showed that the signal was lost at 180% strain due to textile mechanical tear. This amount of elongation was significantly higher than the expected amount of skin deformation around the shoulder joint.

(2) *Cyclical Load Test*: As shown in Fig. 4D, a 5% decrease in the sensor's GF was observed after 1000 cycles. This degradation was caused by the viscoelastic creep in the sensor composite. Due to this phenomenon, under cyclic stress, the sensor's resting length would gradually increase leading to increase in  $C_0$  and decrease in GF. The effect of this signal degradation on long-term kinematics estimation accuracy will be investigated in the future.

Regarding the sensor's mechanical fatigue, Fig. 4E shows a 25% decrease in the sensor's maximum force at the end of the 1000 cycle load test. The large degradation in the sensor's

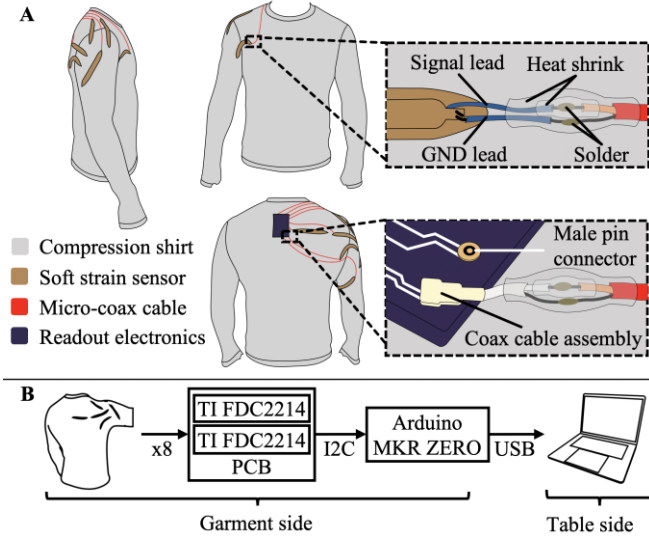


Fig. 5. (A) 2D illustrations of the shirt design with main components color coded and insets detailing sensor to cable and cable to board connections. (B) Data flow schematic.

maximum force was caused by the stress relaxation behavior in the sensor materials. This viscoelastic behavior implied that the sensing shirt would become decreasingly restrictive with continuous usage.

#### IV. SHIRT DESIGN

The garment was designed as a single piece that could be worn as an inner shirt. The base of the garment was an athletic compression shirt. To capture the shoulder kinematics, 8 sensors were sewn onto the shirt around the shoulder joint using an industrial sewing machine with a flat overlock stitch (MB-4DFO, Merrow). When determining the number of sensors, more sensors were preferred with considerations of shirt complexity and electronics limitations. For sensor placement, we wanted to place sensors at locations with maximum elongation and, therefore, maximum capacitance change. To avoid directions of low elongation, sensors were initially placed perpendicular to lines of non-extension [28], which are conceptual lines along the human skin where body movements cause neither stretching nor contraction. The sensor placement was then optimized by iteratively placing the sensors at locations and orientations that yield larger sensor capacitance changes. Fig. 5A illustrates the designed garment with the final sensor placement.

Micro-coaxial (coax) cables (50MCX-37, Molex Temp-Flex) with American wire gauge (AWG) of 42 were used as cables connecting between sensors and the readout electronics. 42 AWG was selected because of the cable sewability and low additive capacitance. These cables minimized parasitic capacitance and crosstalk and were sewn onto the shirt as the looper thread in an overlock stitch. As shown in Fig. 5A insets, sensor-to-cable and cable-to-board electrical connections were made by soldering the sewn micro-coax cable to the sensor's conductive leads and to a coax cable assembly respectively. The coax cable assembly contains an integrated PCB connector harness (X.FL-2LP9-032H1TS-A-(300), Hirose Electric Co Ltd) that can be easily attached or detached to a surface mount male pin connector (X.FL-R-SMT-1(02), Hirose Electric Co Ltd).

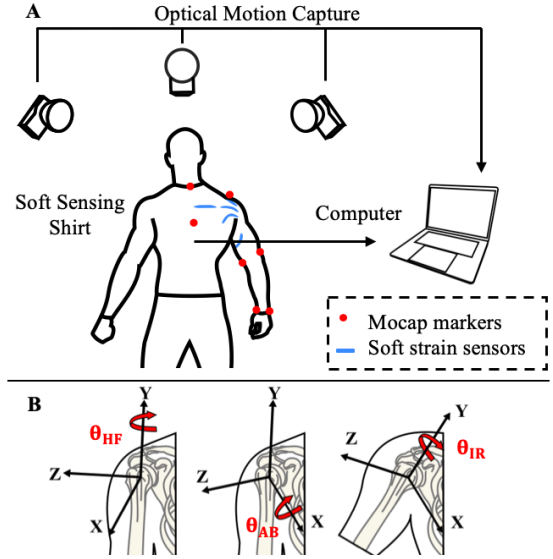


Fig. 6. (A) Illustration of the data collection setup in the motion capture lab. (B) Definition of the Y-X-Y shoulder joint angles.

The readout electronics were composed of a customized PCB and a microcontroller. These two components were attached to the garment using Velcro tapes. The customized PCB digitized sensor capacitance with two off-the-shelf capacitance-to-digital converters (FDC2214Q1, Texas Instruments). Each converter read up to 4 sensors, up to 600 pF, at 35 Hz with 28 bits of resolution. The PCB communicated via I2C protocol to a microcontroller (MKR Zero, Arduino) for data acquisition. The microcontroller was then connected to a laptop via USB for power and data storage. The electronics schematic is shown in Fig. 5B.

#### V. SHOULDER ANGLE AND VELOCITY ESTIMATION

##### A. Data Collection and Preprocessing

In this study, data were collected in a motion capture facility with a single healthy male participant (age: 29, height: 177 cm, weight: 75 kg). Fig. 6A shows the data collection setup. Optical motion capture (mocap) data were collected at 120 Hz using a Qualisys motion capture system with eight infrared cameras. A total of 9 optical tracking markers were attached to the participant on the following anatomical landmarks: C7, T8, IJ, PX, AC, EL, EM, RS, US [29]. The sensing shirt data were recorded simultaneously with the mocap data at 35 Hz. Mocap and sensing shirt signals were synchronized to 35 Hz using MATLAB in post-processing.

Mocap shoulder joint angles were used as the ground truth and were calculated from the three-dimensional marker trajectories using a biomechanical model [29] in Visual3D (C-Motion). As shown in Fig. 6B, mocap humerus joint angles ( $\theta_{HF}$ ,  $\theta_{AB}$ ,  $\theta_{IR}$ ) were defined relative to the thorax in Euler angles (Y-X-Y order). The Y-X-Y Euler angles were recommended by the International Society of Biomechanics and were close to the clinical definitions of degrees of horizontal flexion/extension, abduction/adduction, and internal/external rotation [29]. Ground truth shoulder angular velocities ( $\omega_{HF}$ ,  $\omega_{AB}$ ,  $\omega_{IR}$ ) were calculated by finding time derivatives of the mocap joint angles.

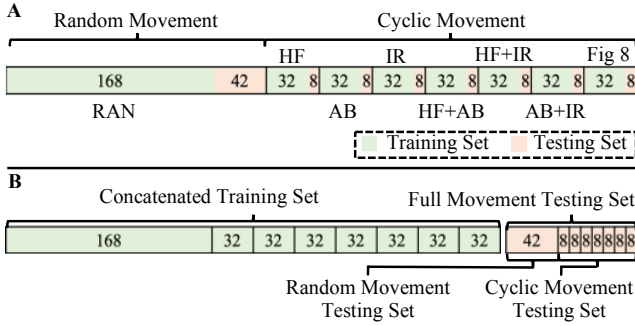


Fig. 7. (A) Experimental protocol with the blocks from left to right representing the recorded shoulder movements in time sequence with numbers showing the duration in seconds. (B) Scheme for training and testing sets where blocks follow the same movement order as (A).

As shown in Fig. 7A, the participant performed 210 seconds of random shoulder movements followed by 280 seconds of cyclic shoulder movements. Cyclic movements consisted repetitive shoulder horizontal flexion/extension (HF), abduction/adduction (AB), internal/external rotation (IR) at 90° abduction, arm circles (HF+AB), HF while IR (HF+IR), AB while IR (AB+IR), and single arm Fig. 8 motion (Fig 8). Each cyclic movement was performed for 20 cycles and 40 seconds in duration. For time series data, train-test splitting must respect the temporal order in which data were collected. Therefore, for each recorded shoulder movement, the first 80% of the data were used as training set and the last 20% were used as testing set. As shown in Fig. 7B, training and testing sets were concatenated into joint training and testing sets. Shoulder kinematics estimation models were built using the concatenated training set and evaluated using the random, cyclic, and full movement testing sets.

### B. Regression Model

To maximize kinematics estimation accuracies, estimation models were trained using the sensing shirt signals from multiple time frames instead of from a single time frame.

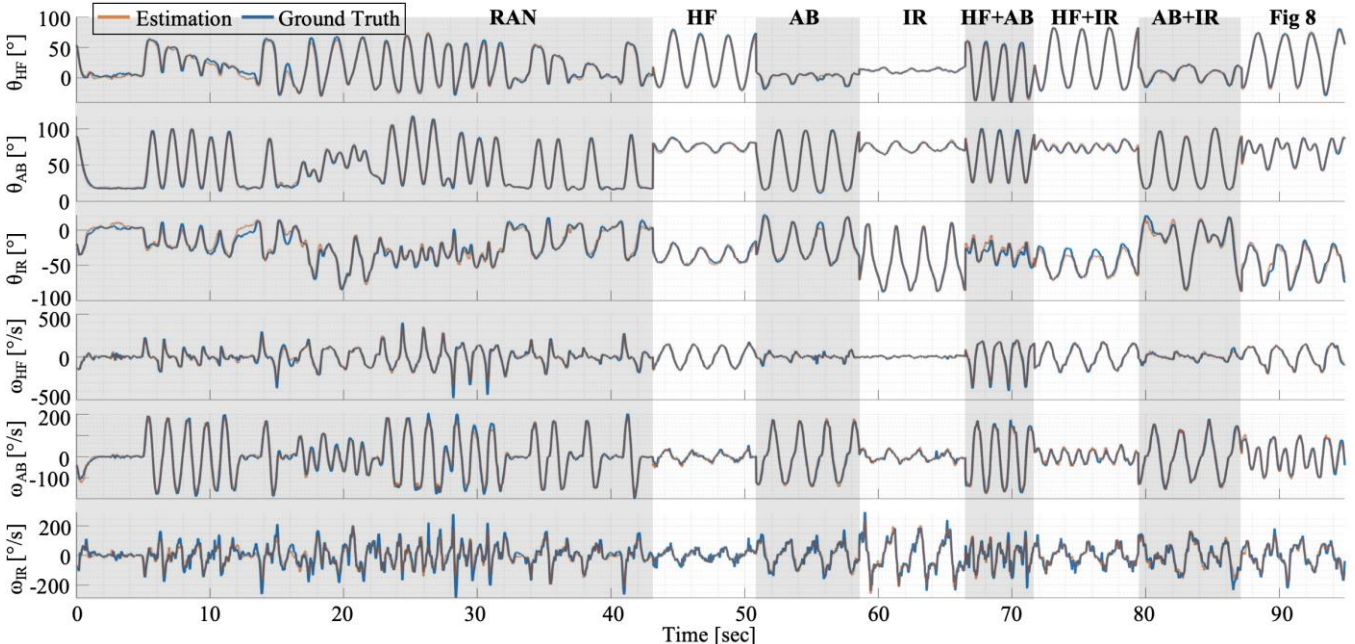


Fig. 8. Visualization of estimation performance on all tested arm movements.

Training with a temporal sequence of shirt signals allowed the regression algorithm to more accurately estimate joint velocities and learn the basic principles of human movements, e.g., human motion should be smooth and continuous. The temporal sequence length was tuned using forward chaining cross-validation. The optimal sequence was from past 5 time frames (0.14 seconds) to future 3 time frames (0.086 seconds). The inclusion of future time frames meant that the estimations would be delayed by 0.086 seconds. Such lag could be reduced at the expense of larger estimation errors.

Estimation models were trained with CatBoost regression [30], a machine learning algorithm based on gradient boosting over decision trees. This algorithm outperformed other tested methods, including linear, 3<sup>rd</sup> order polynomial, k-nearest neighbors, decision tree, and support vector machine regressions, by increasing estimation accuracies by more than 10%. CatBoost regression is a non-parametric method, making no assumption of the underlying mapping function. Such flexibility enabled the algorithm to learn complex relationships between sensor deformation and multi-DOF shoulder movements. Furthermore, CatBoost regression is a single-target method which is restricted to estimating only one variable. To estimate all 6 kinematics variables, 6 CatBoost regression models were chained to sequentially estimate  $\theta_{HF}$ ,  $\theta_{AB}$ ,  $\theta_{IR}$ ,  $\omega_{HF}$ ,  $\omega_{AB}$ , and  $\omega_{IR}$  using the regressor chain method [31]. With this technique, outputs from previous models were included as additional inputs for the current model. Compared to training 6 models in parallel, such reliance on previous regression output improved estimation accuracies by enabling models to learn Euler angles' sequence dependency.

### C. Estimation Performance

The performance of joint angle and velocity estimations were evaluated using RMSEs and normalized RMSEs (NRMSEs) respectively. NRMSEs were used for velocity estimation evaluation for ease of interpretation. NRMSEs were calculated by dividing velocity estimation RMSEs by the velocity min-max ranges obtained from the training set.

The random, cyclic, and full movement test errors are listed in Table 1 and visualized in Fig. 8. Estimation errors of random movements were slightly higher than those of cyclic movements and tracking internal/external rotation was less accurate than tracking the other two DOFs. Because the sensor capacitance change was independent of strain rate, estimation errors appeared to be uncorrelated with joint velocity. However, as shown in Fig. 8, estimation errors of  $\theta_{HF}$  and  $\theta_{IR}$  were larger when  $\theta_{AB}$  was closer to zero. When the second of the three Euler angles approaches zero, the first and third rotation axes are aligned which leads to singularity. At or close to singularity, there could exist multiple valid solutions, thereby contributing to increased errors. Despite the existence of singularity-free representations, such as unit quaternions, Euler angles were used in this study because they were simple and intuitive and required less variables to estimate.

TABLE I. JOINT KINEMATICS ESTIMATION ERRORS

Motion	Joint Angle RMSEs			Joint Velocity NRMSEs		
	$\theta_{HF}$ (°)	$\theta_{AB}$ (°)	$\theta_{IR}$ (°)	$\omega_{HF}$ (%)	$\omega_{AB}$ (%)	$\omega_{IR}$ (%)
Random	3.47	1.88	4.41	2.95	2.98	3.77
Cyclic	2.07	1.42	3.89	1.69	1.99	3.15
Full	2.80	1.64	4.13	2.35	2.49	3.45

Velocity NRMSEs of the full movement corresponded to RMSEs of 18.28 ( $\omega_{HF}$ ), 10.76 ( $\omega_{AB}$ ), and 26.59 ( $\omega_{IR}$ ) deg/sec. Instead of training dedicated regression models, joint velocities could also be estimated by taking time derivatives of joint angle estimates. However, doing so yielded NRMSEs of 3.84% ( $\omega_{HF}$ ), 5.77% ( $\omega_{AB}$ ), and 5.67% ( $\omega_{IR}$ ), worse than the ones reported in Table 1. This performance difference justified the necessity of the dedicated velocity estimation models.

Kinematics estimations took less than 0.12 milliseconds on average using a CPU (2.7GHz quad-core Intel Core i7). This prediction rate was faster than the sampling rate (35 Hz), indicating the capability of estimating in real-time. Besides real-time estimation, future work will also focus on accounting for variation in human body size and sensor position drift from donning/doffing or long-term usage. Potential solution could be characterizing and predicting these variables via data-driven or model-driven approaches or fusing soft sensors with other sensing modalities, like IMUs.

## VI. SENSOR DOWN SELECTION

### A. Methods

The high sensor redundancy generated low estimation errors. However, reducing number of sensors would simplify shirt design and benefit integration with a shoulder assistive robot such as [32]. To this end, the minimal set of required sensors was determined from the current sensor configuration via a recursive feature elimination-based sensor selection analysis. This approach recursively fits estimation models and removes the feature with the lowest importance rank until a pre-determined criterion is met, e.g., meeting specified number of sensors or highest acceptable errors. Each sensor's importance rank was calculated by ranking the sum of its feature importance values across all 6 estimation models. The feature importance value was a built-in attribute of CatBoost regression and described the relevance of each feature in constructing the decision trees. Here, we trained the models

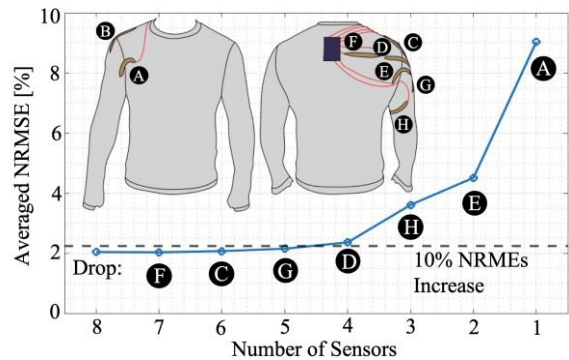


Fig. 9. Result of the RFE-based sensor selection analysis with letter labels indicating the specific sensor dropped at each iteration.

with the concatenated training set, evaluated with the full movement testing set, and terminated with one sensor left.

### B. Results

The average of NRMSEs from all 6 estimation models was used as the evaluation matrix. The analysis result is shown in Fig. 9 with letter labels representing the dropped sensor at each iteration. For example, with 4 sensors, sensors H, E, A, and B were the optimal sensor set with sensors F, C, G, and D dropped from the analysis. Since sensor B was not dropped in any iteration, it was the most significant sensor in this study. Additionally, models trained with 5 sensors (G, D, H, E, and A) still have averaged NRMSE less than 10% increase compared to using all 8 sensors, indicating the feasibility of downsizing sensor set for future shirt designs. The estimation error increased dramatically when the number of sensors was less than 4, indicating the need to have more sensors than the number of output DOFs.

In future work, this feature selection analysis can be adapted to find optimal sensor configuration for specified arm movements or DOFs. This adaptation can be achieved by training with data representative of interested movements or by using an evaluation matrix that only includes interested DOFs. Furthermore, to find more generalizable optimal sensor locations, the analysis needs to be trained with data collected from both genders and participants with different body sizes

## VII. CONCLUSION

In summary, we presented a sensing shirt based on soft capacitive strain sensors capable of accurately estimating shoulder joint angles and angular velocities in 3 DOFs for both arbitrary and rhythmic arm movements. Using RFE based sensor selection analysis, we developed a tool for finding optimal sensor placements. These preliminary results motivate further study to investigate the performance of the shirt under more practical applications. In particular, it will be interesting to study the effects of long-term usage, donning/doffing, and variability in human body size and shape. More specifically, understanding and compensating for sensor to skin and skin to skeleton movements are important for further advancement of wearable motion tracking.

## ACKNOWLEDGMENT

The authors thank Andreas Rousing, Brice Iwangou, Vinicius Cene, Diana Wagner, Megan Clarke, Jonathan Foster, Carolina Correia, and Ciaran O'Neill for their support.

## REFERENCES

- [1] J. Kim et al., "Reducing the metabolic rate of walking and running with a versatile, portable exosuit," *Science*, vol. 365, no. 6454, pp. 668–672, 2019.
- [2] K. Little et al., "IMU-based assistance modulation in upper limb soft wearable exosuits," *2019 IEEE 16th Int Conf Rehabilitation Robotics ICORR*, vol. 00, pp. 1197–1202, 2019.
- [3] Y. Tian, X. Meng, D. Tao, D. Liu, and C. Feng, "Upper limb motion tracking with the integration of IMU and Kinect," *Neurocomputing*, vol. 159, pp. 207–218, 2015.
- [4] S. Zihajehzadeh and E. J. Park, "A Novel Biomechanical Model-Aided IMU/UWB Fusion for Magnetometer-Free Lower Body Motion Capture," *IEEE Transactions Syst Man Cybern Syst*, vol. 47, no. 6, pp. 927–938, 2017.
- [5] D. Roetenberg, H. Luinge, and P. Slycke "Xsens MVN: Full 6DOF Human Motion Tracking Using Miniature Inertial Sensors," XSENS TECHNOLOGIES white paper
- [6] A. Filippeschi, N. Schmitz, M. Miezal, G. Bleser, E. Ruffaldi, and D. Stricker, "Survey of Motion Tracking Methods Based on Inertial Sensors: A Focus on Upper Limb Human Motion," *Sensors*, vol. 17, no. 6, p. 1257, 2017.
- [7] G. Ligorio and A. Sabatini, "Dealing with Magnetic Disturbances in Human Motion Capture: A Survey of Techniques," *Micromachines-basel*, vol. 7, no. 3, p. 43, 2016.
- [8] S. Madgwick, A. Harrison, and R. Vaidyanathan, "Estimation of IMU and MARG orientation using a gradient descent algorithm," *2011 IEEE Int Conf Rehabilitation Robotics*, pp. 1–7, 2011.
- [9] C. Combettes and V. Renaudin, "Delay Kalman Filter to Estimate the Attitude of a Mobile Object with Indoor Magnetic Field Gradients," *Micromachines-basel*, vol. 7, no. 5, p. 79, 2016.
- [10] F. Wittmann, O. Lamercy, and R. Gassert, "Magnetometer-Based Drift Correction During Rest in IMU Arm Motion Tracking," *Sensors*, vol. 19, no. 6, p. 1312, 2019.
- [11] Y. Mengüç et al., "Soft Wearable Motion Sensing Suit for Lower Limb Biomechanics Measurements," *2013 IEEE Int Conf Robotics Automation*, pp. 5309–5316, 2013.
- [12] Y. Mengüç et al., "Wearable soft sensing suit for human gait measurement," *Int J Robotics Res*, vol. 33, no. 14, pp. 1748–1764, 2014.
- [13] D. Kim, M. Kim, J. Kwon, Y.-L. Park, and S. Jo, "Semi-Supervised Gait Generation With Two Microfluidic Soft Sensors," *IEEE Robotics Automation Lett*, vol. 4, no. 3, pp. 2501–2507, 2018.
- [14] M. Totaro et al., "Soft Smart Garments for Lower Limb Joint Position Analysis," *Sensors*, vol. 17, no. 10, p. 2314, 2017.
- [15] C. R. Walker and I. A. Anderson, "Monitoring diver kinematics with dielectric elastomer sensors," pp. 1016307–1016307–11, 2017.
- [16] J.-B. Chossat, Y. Tao, V. Duchaine, and Y.-L. Park, "Wearable Soft Artificial Skin for Hand Motion Detection with Embedded Microfluidic Strain Sensing," *2015 IEEE Int Conf Robotics Automation ICRA*, pp. 2568–2573, 2015.
- [17] Y. Zhou et al., "Soft Robotic Glove with Integrated Sensing for Intuitive Grasping Assistance Post Spinal Cord Injury," *2019 Int Conf Robotics Automation ICRA*, vol. 00, pp. 9059–9065, 2019.
- [18] S. Xu et al., "Biocompatible Soft Fluidic Strain and Force Sensors for Wearable Devices," *Adv Funct Mater*, vol. 29, no. 7, p. 1807058, 2019.
- [19] T.-W. Shyr, J.-W. Shie, C.-H. Jiang, and J.-J. Li, "A Textile-Based Wearable Sensing Device Designed for Monitoring the Flexion Angle of Elbow and Knee Movements," *Sensors*, vol. 14, no. 3, pp. 4050–4059, 2014.
- [20] H. Lee, J. Cho, and J. Kim, "Printable Skin Adhesive Stretch Sensor for Measuring Multi-Axis Human Joint Angles," *2016 IEEE Int Conf Robotics Automation ICRA*, pp. 4975–4980, 2016.
- [21] D. Kim, J. Kwon, S. Han, Y.-L. Park, and S. Jo, "Deep Full-Body Motion Network for a Soft Wearable Motion Sensing Suit," *IEEE ASME Transactions Mechatronics*, vol. 24, no. 1, pp. 56–66, 2019.
- [22] S. Han, T. Kim, D. Kim, Y.-L. Park, and S. Jo, "Use of Deep Learning for Characterization of Microfluidic Soft Sensors," *IEEE Robotics Automation Lett*, vol. 3, no. 2, pp. 873–880, 2018.
- [23] B. Oldfrey, R. Jackson, P. Smitham, and M. Miodownik, "A Deep Learning Approach to Non-linearity in Wearable Stretch Sensors," *Frontiers Robotics Ai*, vol. 6, p. 27, 2019.
- [24] A. Atalay et al., "Batch Fabrication of Customizable Silicone-Textile Composite Capacitive Strain Sensors for Human Motion Tracking," *Adv Mater Technologies*, vol. 2, no. 9, p. 1700136, 2017.
- [25] E. W. Obropta and D. J. Newman, "Skin Strain Fields at the Shoulder Joint for Mechanical Counter Pressure Space Suit Development," *2016 IEEE Aerosp Conf*, pp. 1–9, 2016.
- [26] A. R. Tilley and H. Dreyfuss, *The measure of man and woman: human factors in design*. Wiley, 2001.
- [27] J. C. Otis, R. F. Warren, S. I. Backus, T. J. Santner, and J. D. Mabrey, "Torque production in the shoulder of the normal young adult male," *Am J Sports Medicine*, vol. 18, no. 2, pp. 119–123, 1990.
- [28] A. S. Iberall, "The Use of Lines of Nonextension to Improve Mobility in Full-Pressure Suits," *AMRL-TR. Aerosp. Med. Res. Lab.*, pp. 1–35, Nov. 1964.
- [29] G. Wu et al., "ISB recommendation on definitions of joint coordinate systems of various joints for the reporting of human joint motion—Part II: shoulder, elbow, wrist and hand," *J Biomech*, vol. 38, no. 5, pp. 981–992, 2005.
- [30] E. S. Xioufīs, W. Groves, G. Tsoumakas, and I. P. Vlahavas, "Multi-label classification methods for multi-target regression," *CoRR*, vol. abs/1211.6581, 2012.
- [31] A. Dorogush, V. Ershov, and A. Gulin, "CatBoost: Gradient boosting with categorical features support," in *Proc. Workshop ML Syst. Neural Inf. Process. Syst. (NIPS)*, 2017, pp. 1–7.
- [32] C. T. O'Neill, N. S. Phipps, L. Cappello, S. Paganoni, and C. J. Walsh, "A soft wearable robot for the shoulder: Design, characterization, and preliminary testing," *2017 Int Conf Rehabilitation Robotics ICORR*, vol. 2017, pp. 1672–1678, 2017.